Tidal effects in binary neutron star coalescence

Tidal effects in binary neutron star coalescence

Sebastiano Bernuzzi[1], Alessandro Nagar[2], Marcus Thierfelder[1], and Bernd Brügmann[1]
[1] *Theoretical Physics Institute, University of Jena, 07743 Jena, Germany and*
[2] *Institut des Hautes Etudes Scientifiques, 91440 Bures-sur-Yvette, France*
(Dated: May 16, 2012)

We compare dynamics and waveforms from binary neutron star coalescence as computed by new long-term ($\sim$ 10 orbits) numerical relativity simulations and by the tidal effective-one-body (EOB) model including analytical tidal corrections up to second post-Newtonian order (2PN). The current analytic knowledge encoded in the tidal EOB model is found to be sufficient to reproduce the numerical data up to contact and within their uncertainties. Remarkably, no calibration of any tidal EOB free parameters is required, beside those already fitted to binary black holes data. The inclusion of 2PN tidal corrections minimizes the differences with the numerical data, but it is not possible to significantly distinguish them from the leading-order tidal contribution. The presence of a relevant amplification of tidal effects is likely to be excluded, although it can appear as a consequence of numerical inaccuracies. We conclude that the tidally-completed effective-one-body model provides nowadays the most advanced and accurate tool for modelling gravitational waveforms from binary neutron star inspiral up to contact. This work also points out the importance of extensive tests to assess the uncertainties of the numerical data, and the potential need of new numerical strategies to perform accurate simulations.

I. INTRODUCTION

Gravitational waves (GWs) emitted by binary neutron star (BNS) inspiral and coalescence will be detectable by advanced LIGO-VIRGO detectors. The tidal signature in such waves is (mainly) proportional to the *tidal polarizability parameter* μ_2 that yields the ratio between the tidally induced quadrupole moment and the companion's perturbing tidal gradient. The tidal parameter μ_2 depends on the neutron star equation of state (EOS) and it is related to the relativistic generalization of the Newtonian, dimensionless, Love number [1–5] k_2 as $\mu_2 = 2/(3G)k_2R^5$, where R is the star radius and G the Newton constant. The late-inspiral part of the GW signal, where tidal effects are stronger, can be used to measure the tidal Love number and thus to extract information about the nuclear EOS. A recent study [6] of the measurability of $G\mu_2$, based on the tidal extension [7] of the effective-one-body (EOB) model [3, 8–11], has shown that from a detection of GWs up to merger all normal matter content ($npe\mu$) EOS with maximum mass $\gtrsim 1.97\ M_\odot$ can be distinguished at 95% confidence with signal-to-noise (SNR) ratio 16 and for any physical mass ratio [1].

Accurate theoretical modelling of GWs from BNS coalescence is a challenging task. High post-Newtonian (PN) tidal corrections and resummation techniques are needed to push the validity of the (semi) analytical models up to contact. Next-to-leading order (NLO, fractional 1PN accuracy) [7] (then confirmed in [12]) and next-to-next-to-leading-order (NNLO, fractional 2PN accuracy) relativistic corrections to the tidal interaction energy have been computed recently using effective-field-theory techniques [13]. Fractional 1PN tidal corrections to the waveform were also obtained in [14]. The high-PN tidal corrections effectively amplify the magnitude of leading-order tidal effects, and are now incorporated in the tidal EOB model [6, 7, 15], which is currently the most sophisticated analytical tool available to model the dynamics and waveforms of neutron star (or even mixed) binaries up to contact.

Numerical relativity (NR) simulations are the fundamental tool to compute the dynamics and waveform of the last few orbits of a coalescing BNS system. NR data can be used to calibrate yet uncalculated higher-order tidal effects and to tests the reliability of the analytical models. To date, however, only few works have explored this important problem [16–18].

A first comparison [16] between waveforms from three-orbits NR simulations and the standard, point-mass, Taylor-T4 PN approximant, pointed out that the dephasing accumulated during the last orbits up to merger can be observed and used to constrain the EOS. As discussed there, a major limitation of that work was probably given by the length of the NR data available at the time.

Long-term (nine and eleven orbits) BNS numerical simulations were presented in Refs. [17, 19], and compared there with the prediction of the tidal EOB model. By performing a gauge-invariant and frequency-based analysis of the phasing, it was found that the tidal interaction predicted by the numerical simulation is important even in the early part of the signal. To model it analytically, it was necessary to introduce effective fractional 2PN tidal corrections to the EOB model, yielding an amplification of the analytically predicted tidal effects [7], via the free parameter $\bar{\alpha}_2$; the simulations con-

[1] On the contrary, if only the early inspiral waveform is considered, i.e. only GW frequencies $\lesssim$ 450 Hz (for a BNS with individual masses 1.4 $M_\odot$) it is not possible to measure $G\mu_2$ with sufficient accuracy to discriminate among different EOS [5].

strained it [2] in the range $40 \lesssim \bar{\alpha}_2 \lesssim 100$. That analysis also pointed out that a more detailed analysis of finite-resolution uncertainties on long-inspiral BNS waveforms was needed to correctly estimate the magnitude of tidal effects.

Recently, this important task was undertaken in [18], that presented the first comprehensive analysis of the uncertainties on the waveforms due to truncation and finite extraction error in a nine-orbit BNS simulation. In the same work, NR waveforms were compared to the tidal T4 approximant [5] including also NLO tidal corrections [7, 12, 14]. Significant effects on the phasing due to high-order tidal effects were observed in the "best data" (extrapolated from various resolutions), although a more conservative error estimate did not allow to distinguish higher-order tidal effects.

Motivated by these works and by the last analytical results of [13], we address in this paper the following question: Is the current analytical knowledge necessary and sufficient to reproduce NR data within their uncertainties?

We present results about new NR long-term simulations and their comparison with the up-to-date EOB model [7, 15] which includes the NNLO tidal corrections of [13]. Two different sets of simulations of the same initial data are considered and some difficulties in obtaining NR data of sufficient accuracy are pointed out. We experimentally estimate the contact frequency of the binary, a fundamental information for a comparison with analytical models. NR data are then compared to the EOB model by carefully taking into account their uncertainties. We make use of the gauge-invariant relation between the (reduced) binding energy E and the (reduced) angular momentum j of the system in order to analyse the dynamics of the binary [20]. The phasing of the waveforms is studied both in the time domain and by means of a gauge-invariant and frequency-based approach which does not require to fix any relative (phase and time) alignment between the waveforms [19].

The paper is organized as follows. In Sec. II the tidal EOB model used here is reviewed. In Sec. III the numerical simulations are presented. The EOB/NR comparison is discussed in Sec. IV. Concluding remarks are in Sec. V. We use units $G = c = M_\odot = 1$, unless otherwise stated.

II. TIDAL 2PN EOB MODEL

The tidal extension of the EOB model of the binary dynamics has been defined in Ref. [7] and then improved in Ref. [13] and [6] to include fractional 2PN corrections in the tidal part of the EOB potential $A(r)$. In particular, we address the reader to Appendix A of Ref. [6] for a collection of ready-to-use formulas that define the EOB dynamics and waveforms including fractional 2PN tidal effects. Here we only summarize the main points.

The EOB radial potential has the form

$$A(u) = A^0(u) + A^{\rm tidal}(u), \tag{1}$$

where $u \equiv 1/r = GM/(c^2 r_{\rm AB})$ is the Newtonian potential, $M = M_A + M_B$ the total mass, $r_{\rm AB}$ the relative separation, $A^0(u)$ denotes the point-mass potential and $A^{\rm tidal}(u)$ is the supplementary tidal contribution of the form

$$A^{\rm tidal}(u) = \sum_{\ell=2}^{4} -\kappa_\ell^T u^{2\ell+2} \hat{A}^{(\ell)}_{\rm tidal}(u). \tag{2}$$

The point-mass potential is defined using the usual Padé resummation of the 5PN Taylor expansion of the A function with the 4PN and 5PN EOB parameters (a_5, a_6), $A^0(u) = P^1_5[1-2u+2\nu u^3+a_4\nu u^4+a_5\nu u^5+a_6\nu u^6]$, where $a_4 = 94/3-(41/32)\pi^2$, $\nu = M_A M_B/M^2$, and P^n_m denotes an (n,m) Padé approximant. Following the finding of Ref. [3] (then substantially confirmed by Ref. [21]) we fix the free EOB parameters to the the values $a_5 = -6.37$ and $a_6 = +50$ which lie within the extended region in the (a_5, a_6) plane yielding a good fit of the binary black hole equal-mass simulations.

In the tidal contribution, Eq. (2), the terms $\kappa_\ell^T u^{2\ell+2}$ represent the leading-order (LO) tidal interaction, while the additional factor $\hat{A}^{(\ell)}_{\rm tidal}(u)$ takes into account the effect of distance dependent, higher-order relativistic contributions to the dynamical tidal interactions: 1PN (first-order in u, or next-to-leading order, NLO), 2PN (of order u^2, or next-to-next-to-leading order, NNLO), etc. The dimensionless EOB tidal parameter κ_ℓ^T is related to the tidal polarizability coefficients $G\mu_\ell^{A,B}$ of each neutron star as

$$\kappa_\ell^T \equiv \kappa_\ell^A + \kappa_\ell^B \tag{3}$$

where

$$\kappa_\ell^A \equiv (2\ell-1)!! \frac{M_B}{M_A} \frac{G\mu_\ell^A}{(GM/c^2)^{2\ell+1}}. \tag{4}$$

Here we take advantage of the new analytical results of Ref. [13] and we use the newly computed expressions of $\hat{A}^{(\ell)}_{\rm tidal}(u)$ for $\ell = 2$ and $\ell = 3$ at NNLO accuracy. Focusing on the most relevant equal-mass case ($\nu = 1/4$), the relativistic correction to the tidal potential reads

$$\hat{A}^{(\ell)}_{\rm tidal}(u) = 1 + \alpha_1^{(\ell)} u + \alpha_2^{(\ell)} u^2, \tag{5}$$

where the coefficients $\alpha^{(\ell)}_{1,2}$ are, in this particular case, pure numbers. Specializing to the equal-mass case Eqs. (6.9)-(6.10) and Eqs. (6.21) and (6.22) of Ref. [13]

[2] A similar conclusion, $\bar{\alpha}_2 \sim 40$, was also reached in [7] using non-conformally-flat, NR stationary BNS sequencies.

we obtain

$$\hat{A}^{(2)}_{\rm tidal}(u) = 1 + \frac{5}{4}u + \frac{85}{14}u^2, \tag{6}$$

$$\hat{A}^{(3)}_{\rm tidal}(u) = 1 + \frac{7}{4}u + \frac{257}{48}u^2, \tag{7}$$

$$\hat{A}^{(4)}_{\rm tidal}(u) = 1, \tag{8}$$

where we indicated explicitly the absence of (yet uncomputed) higher-order corrections to the $\ell = 4$ relativistic contribution. The EOB waveform and radiation reaction is computed as in Refs. [19] and takes explicitly into account the 1PN tidal corrections of [14] (see Appendix A of [6] for the precise definition of the EOB waveform with tidal corrections).

Equations (6)-(8) define the most advanced tidal EOB model based on analytical information only. In Ref. [19] a slightly simplified representation of the functions $\hat{A}^{(\ell)}_{\rm tidal}$ was used. Since at the time the NNLO calculation was not completed yet, and only $\alpha^{(2)}_1 = 5/4$ was known, one was using the following NNLO effective expression for the relativistic tidal corrections

$$\hat{A}^{(\ell)}_{\rm tidal} = 1 + \bar{\alpha}_1 u + \bar{\alpha}_2 u^2, \tag{9}$$

with $\bar{\alpha}_1 \equiv \alpha^{(2)}_1 = 5/4$ fixed to be the *same* for $\ell = 2, 3, 4$ and $\bar{\alpha}_2$ taken as a *free* effective parameter (for all ℓ's) to be fitted for by comparison with NR simulations. Although in the following we shall mainly focus on the purely analytical 2PN tidal EOB model defined by Eqs. (6)-(7), we shall also contrast some predictions of the *effective* 2PN EOB model given by Eq. 9 with the numerical data.

The last important concept we want to remember is the definition of *contact* between the two stars. This quantity is important because the analytical model ceases, in principle, to be valid after this moment. Such a formal contact moment was introduced in Eqs. (72) and (77) of [7] by the condition that the EOB radial separation r_{AB} becomes equal to the sum of the tidally deformed radii of the two stars, namely

$$r^{\rm contact}_{AB} = \left(1 + h^A_2 \epsilon_A(r^{\rm contact}_{AB})\right) R_A + A \leftrightarrow B, \tag{10}$$

where $\epsilon_A(r_{AB}) = M_B R^3_A/(r^3_{AB} M)$ is the dimensionless parameter controlling the LO strength of the tidal deformation of body A by its companion B, R_A is the star radius and h^A_2 is the shape Love number [15, 22]. The dimensionless quantity h^A_2 is of order unity, but one is expecting it to be a function of the relative separation r, that increases as r decreases (this was found in a related black-hole study [22]). In Ref. [19] it was found that the effective value $h^{\rm eff}_2 = 3$ was necessary to allow this EOB-predicted contact to occurr always before the NR-defined merger. We shall briefly comment in Sec. IV about the magnitude of the amplification needed on h_2 so to reconcile the EOB contact defined by Eq. (10) with a certain NR-defined contact.

TABLE I. Summary of the grid configurations and of the runs. Columns: name of the configuration, maximum refinement level, minimum moving level, number of points per direction in the moving levels, resolution per direction in the level $l = l_{\rm max}$, number of points per direction in the non-moving levels, resolution per direction in the level $l = 0$.

run	$l_{\rm max}$	$l^{\rm mv}$	$N^{\rm mv}_{\rm xyz}$	$h_{\rm l_{max}}$	$N_{\rm xyz}$	h_0
L	7	4	100	0.1875	160	24
M	7	4	128	0.1466	176	18.75
H	7	4	160	0.1172	212	15

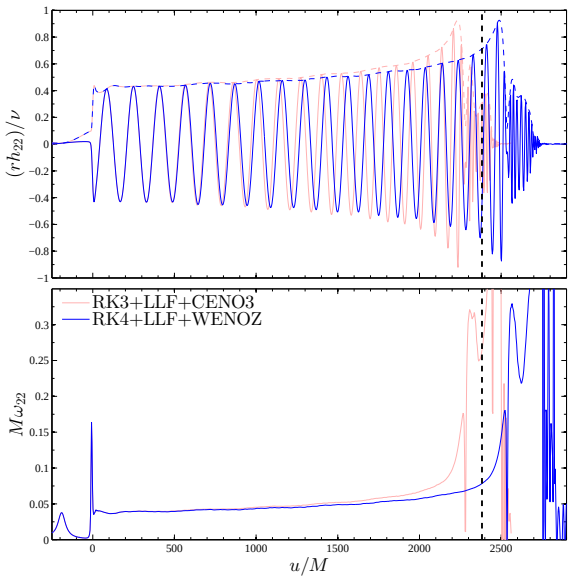

FIG. 1. (color online) Numerical quadrupolar gravitational waveform extracted at the outermost radius $r_{\rm obs} = 750 = 247.55M$ for the CENO and WENO data (run H). Top: real part and amplitude (dashed lines). Bottom: frequency. The vertical lines mark the contact of the WENO data.

III. NUMERICAL SIMULATIONS

Target waveforms for the comparison with different analytical predictions are computed via NR simulations like those presented in great detail in [18]. While NR simulations of BNS have reached a certain maturity (see [23] for the most recent review), intrinsic difficulties in the treatment of general relativistic hydrodynamics (GRHD) make the numerical calculations of small effects in long simulations still very challenging. Note that the study of tidal effects in the late inspiral requires to resolve (at least) dephasing of $\lesssim 0.5$ *rad* over ten cycles. In particular the numerical viscosity of high-resolution-shock-capturing scheme (HRSC) typically employed, is strongly dependent on the reconstruction scheme (cell-interfaces interpolation), and plays an important role in the accu-

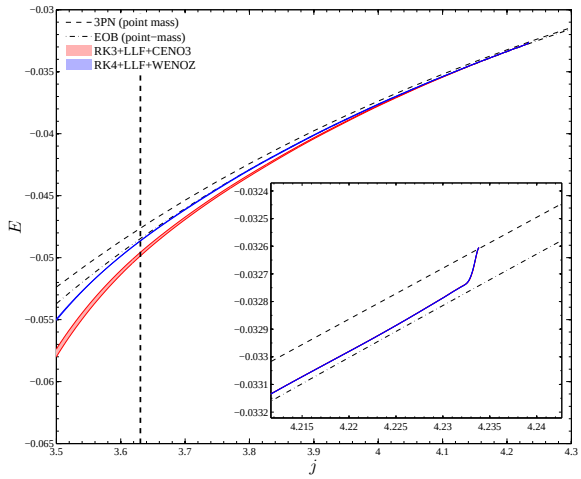

FIG. 2. (color online) Numerical dynamics: $E(j)$ curves for two series of simulation (CENO and WENO data), and for two point-mass analytical models (EOB resummed and "canonical" Taylor-expanded 3PN). The vertical dashed line marks the angular momentum at contact.

racy of the simulations, see e.g. [24, 25]. While partially under control in short (three orbits) runs by the use of 3rd order reconstructions, long term simulations such those presented here are challenging, also due to the computational cost of extensive testing.

In this work we consider long-term evolutions ($\sim$10 orbits) of an equal-mass conformally-flat (CF) and irrotational initial configuration of Arnowitt-Deser-Misner (ADM) mass $M^0_{\rm ADM} = 3.00506(2)$ and angular momentum $J^0_{\rm ADM} = 9.716(1)$. The initial separation is $d \sim 50$ associated with GW frequency of $\sim 394\ Hz$. The fluid is described by a Γ-law EOS ($\Gamma = 2$) and isentropic evolution were considered as in [18]. The baryonic mass of each star is $M_{\rm b} = 1.62500(0)$, the gravitational mass of each star in isolation is $M/2 = M_A = M_B = 1.51483(7)$, radius and compactness are respectively $R = 10.82065(0)$ and $\mathcal{C} = 0.14$. The corresponding $\ell = 2$ dimensionless Love number is $k_2 = 0.07890(1)$ and the $\ell = 2$ shape Love number is $h_2 = 0.8699$. The initial configuration [26] is computed with the LORENE library and publicly available, and was already considered in Refs. [17–19].

Evolutions were performed with the BAM code described in [25, 27, 28]. Here we mention the GRHD is handled with finite-differencing HRSC based on primitive reconstruction, the Local-Lax-Friedrichs (LLF) central scheme for the numerical fluxes and Runge-Kutta time integrators, see e.g. [29]. Cartesian grids and Berger-Oliger adaptive-mesh-refinement ("moving boxes" technique) are used. The grid setup, resolutions, gauge parameters, and finite differencing stencils for the metric sector are exactly the same as the convergent series discussed in [18], they are listed for completeness in Table I.

We point out here that focusing on isentropic evolutions is justified by the following facts: (i) physically, BNS evolutions are expected to be isentropic up to contact; (ii) any analytic model can not describe non-isentropic effects (e.g. shock heating); (iii) previous works demonstrated [19, 25] that considering non-isentropic evolutions actually leads to *smaller* tidal effects.

Two series of simulations were performed: one is the convergent series presented in [18], where the HRSC employs the (formally) 3rd order convex-essentially-non-oscillatory (CENO3) for primitive reconstruction and a 3rd order Runge-Kutta scheme. The second series is computed with the same setup except the use of the (formally) 5th order weighted-essentially-non-oscillatory (WENOZ) method of [30] and a Runge-Kutta scheme of 4th order. In [18] it was presented a detailed analysis of the uncertainties that affect the waveform due to truncation and finite-extraction errors; the new data computed for this work show analogous features. However, we observed differences between the two data sets. For a given resolution, the merger in the CENO data occurs earlier than in the WENO data. The dominant multipole $\ell = m = 2$ of the metric waveforms, h_{22}, obtained from the two different setup is displayed in Fig. 1. In abscissa we use the retarded time $u \equiv t - r_*$, where $r_* = r_{\rm S} + 2M_{\rm ADM}\log(r_{\rm S}/(2M_{\rm ADM}) - 1)$, and $r_{\rm S}$ is the Schwarzschild radius corresponding to the isotropic (coordinate) radius r. The waveforms are extracted at the outermost radius $r = 750 = 247.55M$. The simulations compute waveforms from the Newman-Penrose scalar ψ_4, that is then decomposed in spherical harmonics modes, $\psi_4^{\ell m}$. The metric multipoles $h_{\ell m}$ are calculated from the $\psi_4^{\ell m}$ by integrating the relation $\psi_4^{\ell m} = \ddot{h}_{\ell m}$. To do the integration, we use the frequency-domain procedure of [31] with a low-frequency cut off at $\omega_0 = 0.02/M$. The signal is integrated from the very beginning of the simulation, in order to include also the initial burst of radiation related to the use of CF initial data. This radiation is often called (somehow improperly) "junk" radiation. Note that in the text for brevity we consider the metric waveform multiplied by the extraction radius without explicitly changing the notation, i.e. $h_{\ell m} \equiv r h_{\ell m}$. As it is clear from the figure, at a given resolution, CENO and WENO waveforms accumulate a significant relative dephasing towards merger; uncertainties due to the HRSC numerical viscosity become larger as the simulation time advances and eventually dominant over truncation (and finite extraction) errors towards contact ($M\omega_{22} \sim 0.07$ [18], see below for an estimate of the GW frequency of the contact), where any convergent behavior is lost. For both data sets the higher the resolution, the later is the merger [18, 25]. In practical terms, Fig. 1 indicates that the differences in the HRSC effectively influence the magnitude of the tidal interaction between the two stars, from a larger value for the CENO data to a smaller one for the WENO data.

This effect can be properly quantified by exploring the actual dynamics of the BNS system so to contrast it with the corresponding point-mass one. An intrinsic, gauge-

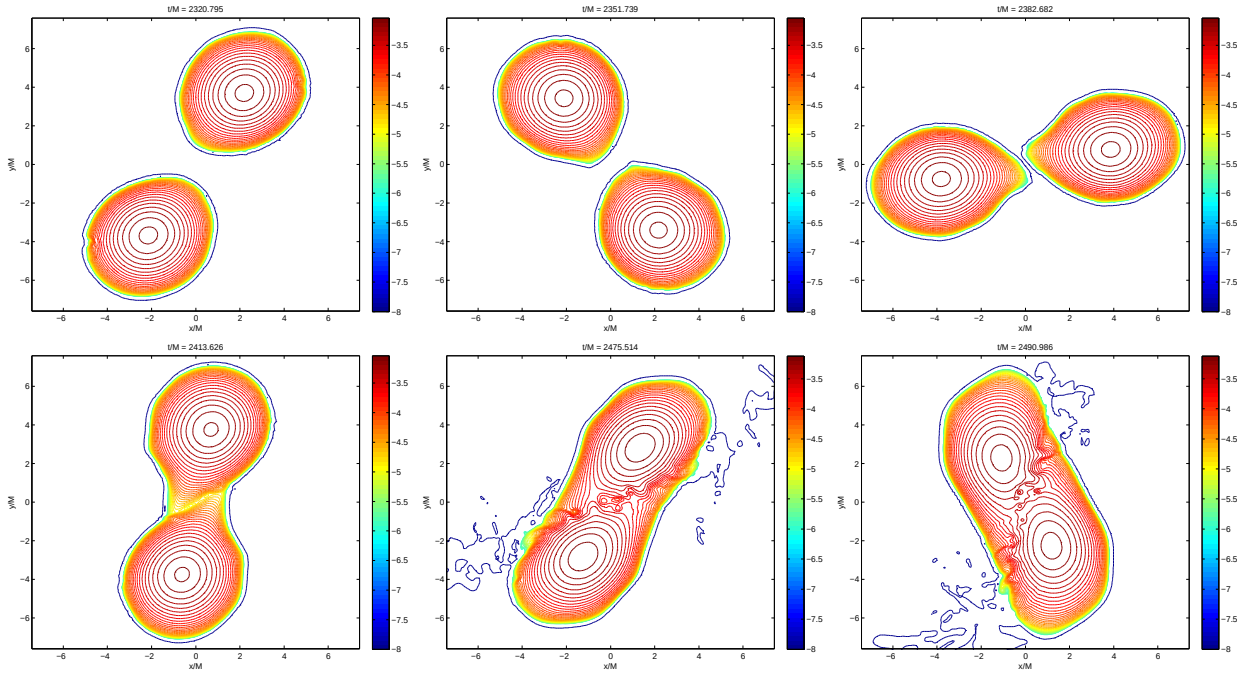

FIG. 3. (color online) Binary dynamics from WENO NR simulations. Contour plot of the rest-mass density on the equatorial plane. The snapshots indicate the contact happens around dynamical time $t_c \approx 2382M$. This dynamical time, corresponding to observer's retarded time $u_c = t - r_*^{\rm obs}$, locates the contact at GW frequency $M\omega_{22}^c \approx 0.078$. Run H.

invariant, way of doing so is by means of the relation between the total energy $\mathcal{E}$ and total angular momentum $\mathcal{J}$ of the system, $\mathcal{E}(\mathcal{J})$. Following Ref. [20] that computed this quantity for binary black hole (BBH) systems, $\mathcal{E}$ and $\mathcal{J}$ are obtained from the NR data as

$$\mathcal{E}^{\rm NR}(u) = \mathcal{E}_0 - \Delta\mathcal{E}^{\rm NR}_{\rm rad}(u)\,, \tag{11}$$

$$\mathcal{J}^{\rm NR}(u) = |\boldsymbol{\mathcal{J}}_0 - \Delta\boldsymbol{\mathcal{J}}^{\rm NR}_{\rm rad}(u)|\,. \tag{12}$$

Here, $\mathcal{E}_0 = M^0_{\rm ADM}/M$ and $\mathcal{J} = J^0_{\rm ADM}/M^2$ are the initial ADM mass and angular momentum expressed in units of the total gravitational mass of the stars in isolation; $\Delta\mathcal{E}^{\rm NR}_{\rm rad}$ and $\Delta\mathcal{J}^{\rm NR}_{\rm rad}$ (expressed in the same units) are the radiated energy and angular momentum between the initial (retarded) time u_0 and u. They are computed from the multipole moments of the metric waveform $h_{\ell m}$ and of its time derivative $\dot{h}_{\ell m}$, as

$$\Delta\mathcal{E}^{\rm NR}_{\rm rad}(u) = \frac{1}{16\pi}\sum_{\ell=2}^{\ell_{\rm max}}\sum_{m=0}^{\ell}\int_{u_0}^{u} du' \left|\dot{h}_{\ell m}(u')\right|^2 \tag{13}$$

$$\Delta\mathcal{J}^{\rm NR}_{z\rm rad}(u) = \frac{1}{16\pi}\sum_{\ell=2}^{\ell_{\rm max}}\sum_{m=1}^{\ell}\int_{u_0}^{u} du' m\Im\left[h_{\ell m}(u')\dot{h}^*_{\ell m}(u')\right]. \tag{14}$$

In Eq. (12) we also included the x, and y component of the angular momentum loss, $\Delta\mathcal{J}^{\rm NR}_x$ and $\Delta\mathcal{J}^{\rm NR}_x$, though, as expected, they are of order 10^{-10} and negligible in practice. For convenience, we work with the binding energy per reduced mass $E \equiv (\mathcal{E} - M)/\mu$ and the dimensionless rescaled angular momentum $j \equiv \mathcal{J}/M\mu$, where $\mu = M_A M_B/M$.

The main panel of Fig. 2 compares the NR relations $E^{\rm NR}(j)$ computed for the two data series (CENO and WENO) with two analytical, point-mass, curves: the canonical PN expanded $E(j)$ relation (see Eq. (5) of [20]), dashed line, and the NR-tuned, EOB resummed one (dash-dotted line), that was found in [20] to show an excellent agreement with corresponding BBH numerical curve [3] (see Fig. 2 of [20], top panel). The $E^{\rm NR}(j)$ curves used here were obtained from waveforms taken at the the outermost extraction radius, $r_{\rm obs} = 750 = 247.55M$, and, for simplicity, by including only the $\ell = m = 2$ multipole in the calculation of Eqs. (11)-(12). To illustrate the influence of the uncertainties due to finite resolution, instead of displaying the NR data as a simple curve, we present them as the shaded band that is included between the medium (run M, bottom border) and high (run H, top border) resolutions. The diagram illustrates that, while the CENO data graze the EOB point-mass curve at the very beginning of the simulation (see inset) they visibly deviate from it after, indicating the presence of strong

[3] Although the canonical PN curve was very close to the CF initial state, it was found to progressively deviate from the numerical calculation, giving then an inaccurate representation of the point-mass dynamics.

tidal effects. On the contrary, the WENO data remain always very close to the point-mass EOB curve, so to be almost indistinguishable on the scale of the main plot.

We experimentally conclude that the more dissipative numerical setup (CENO data) artificially amplifies tidal effects, leading to severe inaccuracies on the waveform phasing. The improvements obtained in the WENO data and the availability of convergence tests and error estimates [18] are crucial for the comparison with the analytical information presented below.

Let us finally briefly comment the inset of Fig. 2, which focuses only on the initial part of the $E^{\rm NR}(j)$ curve. Similarly to the black-hole case (see inset of Fig. 1 of [20]), the initial state of the system is very close to the point-mass, 3PN canonical $E(j)$ curve. Then the effect of the losses due to the junk radiation moves the initial state down, close to the EOB curve. Note in addition that this early-inspiral part the NR curve is *above* the point-mass EOB curve because only the $\ell = m = 2$ mode has been included. We shall explore the effect of the other multipoles in the next Section, in the context of the detailed comparison with the tidal EOB model.

For the comparison with analytical predictions, it is important to have an estimate of some *contact* frequency extracted from the NR data, since the tidal EOB model ceases to be valid after. However, connecting the (local, strong-field) dynamics, parametrized by the dynamical time t, of the two objects with the radiation observed in the wave-zone unambigously, is a non-trivial task. In first approximation, any phenomenon occurring in the strong field region at dynamical time t reaches the observer $r_{\rm obs}$ at retarded time $u = t - r_*(r_{\rm obs})$. For simplicity, in the following we shall assume such relation to connect the two events, though, in doing so, we are neglecting an additional time-delay due to the propagation of the signal in the strong-field region. In Fig. 3 we show snapshots of the rest-mass density in the orbital plane at few dynamical times around the contact of the two stars. The pictures indicates clearly that at $t_{\rm c} \approx 2382M$ the well-known shearing contact is taking place. The corresponding GW frequency is $M\omega_{22}(u_c = 2382M) \approx 0.078$, and the corresponding value of the angular momentum is $j_{\rm c} \approx 3.63$. The latter is shown in the dashed vertical line in Fig. 2. Note that the final merger (e.g, formally defined by the first peak of $|h_{22}|$) occurs later, at $M\omega_{22} \sim 0.13$.

IV. EOB/NR COMPARISON

In this Section we consider only the WENO data and compare them with the tidal EOB model. We present two types of comparisons, one for the dynamics, through the $E(j)$ curve, and one for the phasing. We shall take as "best" (multipolar) waveform the one computed with the highest resolution available and extracted at the outermost radius $r_{\rm obs} = 247.55M$.

A. Dynamics

Let us first compare the NR $E^{\rm NR}(j)$ relation to the corresponding analytical prediction. This is done in the left panel of Fig. 4. Together with the point-mass analytical curves (EOB and canonical 3PN) already shown in Fig. 3, we also display the analytical $E(j)$ EOB curve that includes tidal effects (solid, red online) at NNLO order. The numerical curve (solid, black online) is different from the corresponding band of Fig. 3 in that $\Delta\mathcal{J}^{\rm NR}_{\rm rad}$ and $\Delta\mathcal{E}^{\rm NR}_{\rm rad}$ include all multipolar contributions up to $\ell_{\rm max} = 4$. Note that, although the symmetry of the system implies that all multipoles with odd values of m have to be zero, they are actually nonzero, and are included in the computation of the losses to which they contribute as very small amplitude, structureless, noise. In these simulations, differently from [19], we do not impose rotational ("π") symmetry on the orbital plane, but evolve instead the equations in the whole plane $z > 0$. To give numbers in the $\ell = 2$ case, during the inspiral it is, at maximum, $|\dot{h}_{22}| \sim 5 \times 10^{-3}$, $|\dot{h}_{20}| \sim 2 \times 10^{-5}$ and $|\dot{h}_{21}| \sim 6 \times 10^{-6}$.

Though the $m = 0$ modes are practically negligible during the inspiral, they actually contribute to the initial burst of radiation and thus they must be included in the computation of $E^{\rm NR}(j)$. For example, during this epoch, that lasts for $\sim 25M$, $|\dot{h}_{20}| \sim 0.5 \times |\dot{h}_{22}|$ and $|\dot{h}_{40}| \sim 0.5 \times |\dot{h}_{44}|$. By contrasting the insets of Fig. 3 and of the left-panel of Fig. 4, we observe that the subdominat multipoles drive the NR curve not only below the point-mass curve, but even below the tidal EOB curve [4]. Like in Fig. 3, the dashed vertical line marks the location of the NR-contact. We note in passing that to make the EOB-contact consistent with the NR-defined contact we should replace in Eq. (10) the value $h_2 = 0.8699$ (which would give a EOB contact frequency slightly smaller than the merger frequency [5] $M\omega_{22} \sim 0.094$) with $h_2^{\rm eff} \sim 3.4$, which yields an EOB contact frequency ~ 0.078. This estimate of the deformation of each star coming from actual data is consistent with the guess of Ref. [19] ($h_2^{\rm eff} = 3$), but further work will be needed to understand, numerically, the actual amplification experienced by h_2.

By close inspection of the plot we observe that the NR curve actually change its slope: around $j \sim 3.8$ it lies between the tidal and point-mass curves, while during contact the curve bends again below the tidal EOB one. We argue this behavior is caused by numerical inaccuracies, for example small violations of mass conservation, to which the computation of $E^{\rm NR}(j)$ is extremely sensitive. It was not possible to identify the precise cause, but

[4] The tidal EOB curve is below the corresponding point-mass one indicating that, due to the attractive nature of tidal interaction, the system is gravitationally more bound.

[5] Similarly, the "bare" contact, with $h_2 = 0$, is even closer to the merger, giving $M\omega_{22} \sim 0.106$.

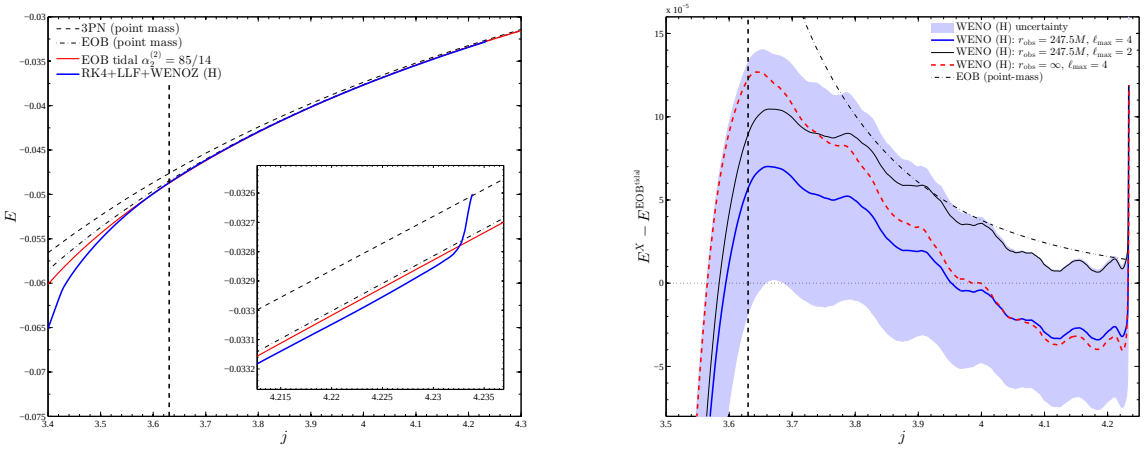

FIG. 4. Comparison between EOB and NR dynamics. Left panel: reduced binding energy (E) versus reduced angular momentum (j) curves. Right panel: differences with the tidal EOB model. The shaded region represents the estimated uncertainties on the "best" numerical curve. Numerical data are consistent with the tidal EOB model.

we mention that it corresponds to a numerical oscillation at the fourth digit of $E^{\rm NR}(j)$.

The differences between numerical data and the analytical predictions are made precise in the right panel of Fig. 4. The four curves represent the four differences $E^X - E^{\rm EOB_{tidal}}$ where the label X indicates in turn: NR (thick, red online) with $\ell_{\rm max} = 4$; NR (thin, black online) with $\ell_{\rm max} = 2$; NR (thick, dashed, black online) with $\ell_{\rm max} = 4$ extrapolated at infinite extraction radius; EOB point-mass (dash-dotted, black online). The shaded region represents the estimated uncertainty affecting the best waveform. It has been obtained by taking into account the following three effects: (i) resolution; (ii) finite extraction radius; (iii) contribution of higher multipoles. To compute it, we first took the following differences between $E^{\rm NR}(j)$ curves: (i) between H and M data, $\Delta E^{\rm HM}$; (ii) between H data extrapolated at infinite extraction radius and at $r_{\rm obs} = 247.55M$, $\Delta E^{\rm H}_{\infty}$. The extrapolation was done from data at $r_{\rm obs} = \{400, 500, 600, 700, 750\}$, aligned using retarded time, taking a quadratic fit; (iii) between H data with $\ell_{\rm max} = 4$ and with $\ell_{\rm max} = 2$, $\Delta E^{\rm H}_{\ell}$. Then the final (conservative) error-bar is obtained as $\Delta^{\rm NR}E(j) = \pm\sqrt{(\Delta E^H_{\infty})^2 + (\Delta E^{\rm HM})^2 + \left(\Delta E^H_{\ell}\right)^2}$. Note that at large values of j (beginning of the simulation) the most relevant uncertainty is the one due to the finite radius and to the choice of $\ell_{\rm max}$; after that, finite-resolution effects become dominant.

The analysis of the dynamics shows that the NR data are *consistent* with the state-of-the-art tidal EOB model, and distinguishable from the point-mass EOB model up to contact ($j_c = 3.62$). Remarkably the NR curves stay very close to the tidal EOB up to $j \sim 3.5$, point at which the differences with the point-mass curves are at least two-sigma beyond the uncertainties.

TABLE II. Phase differences $\Delta\phi = \phi^{\rm EOB} - \phi^{\rm NR}$, with its uncertainty $\sigma_{\Delta\phi}$, accumulated between frequencies $[\omega_1, \omega_2] = [0.041,\ 0.062]/M$ obtained by integrating the difference between the NR Q_ω and some of the EOB curves of Fig. 6: the point-mass, the tidal LO and the 2PN (NNLO) analytical one with $\alpha_2^{(2)} = 85/14$. The error-bar $\pm\sigma_{\Delta\phi}$ is obtained by integrating the shaded region around the NR Q_ω curve in Fig. 6.

EOB model	point-mass	LO tidal	NNLO tidal
$\Delta\phi$ $[rad]$	3.92	1.49	1.06
$\sigma_{\Delta\phi}$ $[rad]$	0.61	0.61	0.61

B. Waveforms and phasing

Let us now compare the waveforms and quantify the phase difference accumulated between NR and EOB data in the last orbits of the inspiral. Focusing on the $\ell = m = 2$ mode, we first present a time domain comparison of the amplitude and frequency, and then switch to a more quantitative analysis of the phasing. Higher multipoles are discussed at the end of the section.

In Fig. 5 we contrast the NR waveform (thin solid line, black online) with 4 different analytical models: the EOB point-mass (no tides, dash-dotted line), the tidal EOB with only LO tidal effects (i.e., we set $\hat{A}^{\rm tidal}_{\ell} = 1$ for all ℓ's in Eq. (2)), dashed, thick curves, blue online), the 2PN-accurate (NNLO) tidal EOB model (solid thick curves, red online) and the PN-expanded Taylor T4 model with leading order tidal effects (see Sec. IIIC of [19]). We show together the gravitational frequency (top left) and waveform modulus (top right) while the corresponding differences (EOB-NR) are exhibited in the bottom panels. The vertical dashed line on each panel indicates the NR

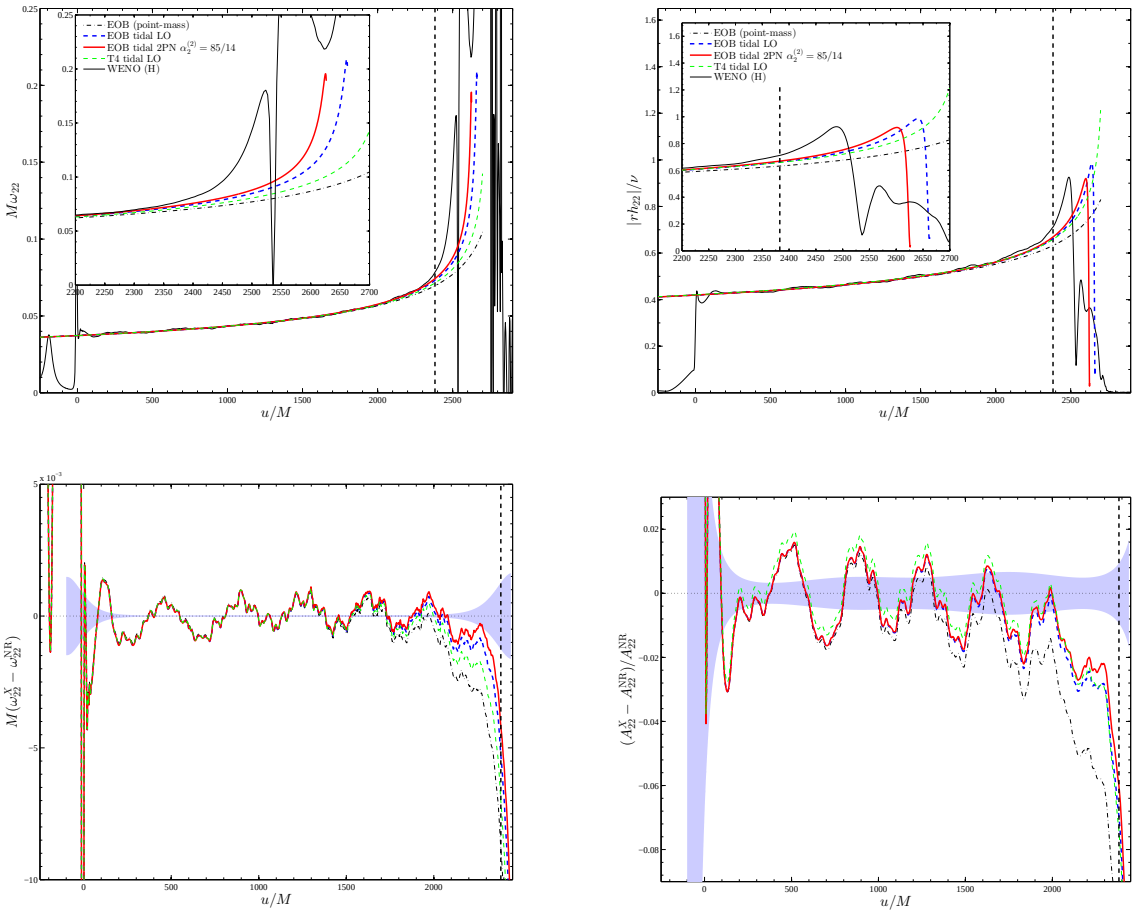

FIG. 5. Comparing numerical and analytical $\ell = m = 2$ waveform: frequency (left panels) and modulus (right panels). The vertical line locates the NR contact. The shaded regions in the bottom panels are error estimates on the NR frequency and modulus.

contact frequency $M\omega_{22}^{c} \approx 0.075$, after which we don't expect any analytical model to be accurate. The relative time, τ and phase, α, shifts that are necessary to align the analytical to the numerical waveform are determined using the procedure described in Sec. VA of Ref. [19], that relies on the minimization of the χ^2 of the phase difference over a certain frequency interval. Here we use the frequency interval $(\omega_1, \omega_2) = (0.038, 0.049)/M$, (corresponding to $(u_1, u_2)/M = (165.8, 1610.9)$, that begins after the initial burst of radiation, so as to remove also possible inaccuracies due to the integration procedure needed to get h_{22} from ψ_4^{22}. The shaded regions in the bottom panels indicate the NR uncertainty, that takes into account finite-extraction radius and finite resolution effects. It is obtained by: (i) Richardson extrapolating the two highest resolutions assuming second order convergence and taking the difference with run H data; (ii) similarly, taking the difference between the NR waveform extrapolated in extraction radius [6] and the one at $r_{\rm obs} = 750$. In practice, for the first half of the simulation ($u \sim 1000M$) the uncertainty is dominated by finite-extraction-radius effects, while later it is the resolution to play the most important role. The two contributions are then summed in quadrature and one takes the $(\pm 1/2)$ of the square root to obtain a two-sided error bar. Note that the finite-resolution uncertainties we quote are consistent with Table II of [18] and provide an average between optimistic and conservative estimate of the errors (obtained respectively by resolution-extrapolated data from five and three simulations with different resolutions).

From the top panel of Fig. 5 one sees visually how the tidal models clearly yield a better agreement with

[6] In Ref. [18] it was shown that in this case phase difference due to finite-radius effects varies between ~ 0.2 rad during the early inspiral to ~ 0.1 rad at merger, while the fractional difference in amplitude varies between 1% and 0.5%.

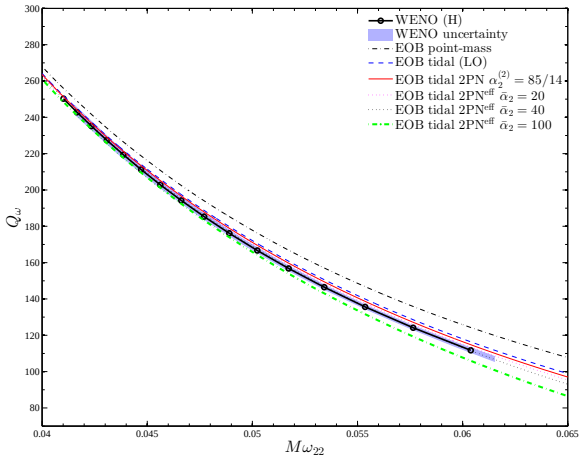

FIG. 6. (color online). Comparison between various EOB Q_ω curves and the NR one. The good visual agreement between the LO and 2PN tidal EOB models and the NR curve highligths the presence of tidal interaction during the inspiral. Note that the effective value $\bar{\alpha}_2 = 100$ used in Ref. [19] is incompatible with the NR curve.

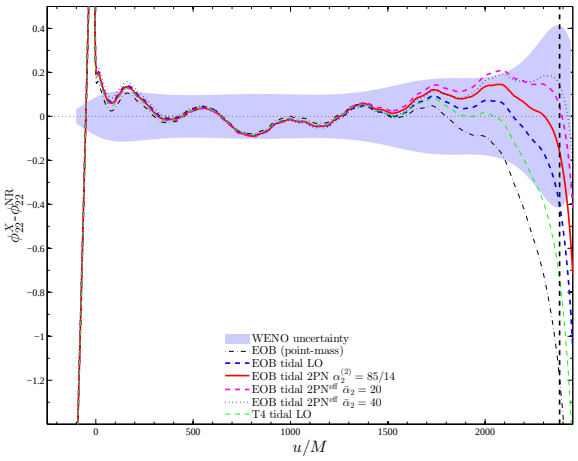

FIG. 7. (color online) Phase difference between various analytical phase and the NR phase. The vertical line indicates the NR contact. The phase difference of $\sim -0.2 rad$ between the 2PN tidal EOB model and the NR waveform is compatible with the error estimates on the latter.

the numerical data than the simple point-mass EOB model [7]. This information is made more quantitative in the the bottom panels, where the point-mass analytical

[7] Note that up to GW frequency $M\omega_{22} \sim 0.1$ the Taylor T4 point-mass phasing agrees very well with the NR one and thus with the NR-tuned EOB point-mass.

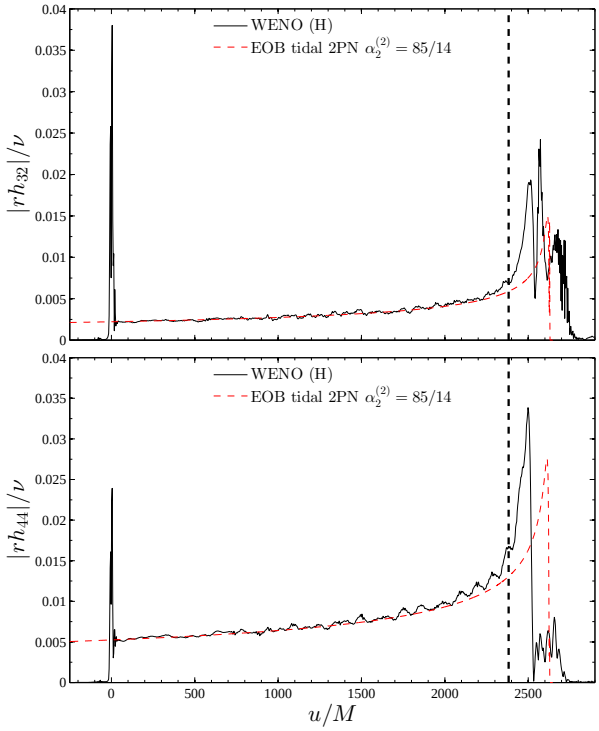

FIG. 8. (color online). Comparing EOB and NR waveform moduli for the most relevant subdominant multipoles h_{23} and h_{44}. The vertical line marks the NR-defined contact time.

prediction is seen to deviate away starting from $2000M$, while the other differences remaining much flatter, and marginally close to the error bar, up to contact. The comparison of Fig. 5 allows us to deduce the presence of tidal effects in the very late part of the inspiral, just before contact. However, it also indicates that this comparison is sensible *at most* to leading-order tidal effects, since, given the uncertainties on the NR data, it is not possible to meaningfully disentangle 1PN and 2PN tidal corrections from the leading-order ones. On these plots, the Taylor T4 PN model with LO tidal corrections looks consistent with the EOB predictions, yielding similar differences with the NR waveform. Note that at the very contact position the frequency and amplitude differences show a clear increasing trend. This might either be due to the "blurred" nature of contact in the NR data, or to the lack of suitably determined next-to-quasi-circular corrections. For simplicity, we will not overtune here more our analytical model and postpone to a future investigation the detailed analysis of these additional effects.

We discuss now the phasing by means of a gauge-invariant and frequency-based analysis employing the $Q_\omega = \omega^2/\dot{\omega}$ function (where we put $\omega \equiv M\omega_{22}$ for simplicity) introduced and used extensively in Ref. [19]. We recall that the meaning of this function is that the

time-domain GW phase $\phi_{(\omega_1,\omega_2)}$ accumulated between frequencies (ω_1,ω_2) is given by the integral $\phi_{(\omega_1,\omega_2)} = \int_{\omega_1}^{\omega_2} Q_\omega d\ln\omega$. Consequently, a change of $Q_\omega(\omega)$ of the order ±1 during a frequency octave $\ln(\omega_2/\omega_1)$ corresponds to a local dephasing (around ω) of $\delta\phi \simeq \pm1$ *rad*. The main advantage of the Q_ω diagnostics is that it is independent of the arbitrary time and phase shifts (τ,α) necessary to compare the waveforms in the time domain.

As in Ref. [19] we cannot compute Q_ω from the raw NR data, but we have fitted the phase of h_{22} with a suitable PN-based expression (see Eqs. (27)-(28) of [19]). Here the best fit is given by using a sixth-order polynomial (in contrast to the fourth-order polynomial employed in [19]) in the variable $x = [\nu(t_m - t)/5]^{-1/8}$ (where t_m is a fitting parameter formally representing the merger time), and the time interval $[t_L, t_R]/M = [965, 2400]$, which corresponds to frequencies $[\omega_L,\omega_R] = [0.042, 0.063]/M$. The Q_ω curve, so obtained, is represented by the thick-solid line with circles in Fig. 6. The shaded region around the curve indicates the uncertainty on the curve as given by $Q_\omega^{\rm NR} \pm \sigma_{Q_\omega^{\rm NR}}$. This numerical uncertainty $\sigma_{Q_\omega^{\rm NR}}$ is estimated by putting together the effect of truncation error, of finite extraction radius, and of the fit. To do so, we first calculated other three Q_ω curves,: one from the waveform of the M run, $Q_\omega^{\rm NR_M}$; another from the waveform of the H run, but extrapolated at infinite extraction radius, $Q_\omega^{\rm NR_H^\infty}$; a third one doing the fit of the H data with the fourth-order polynomial instead of the sixth-order one, $Q_\omega^{\rm NR_{H,\,n=4}}$. We then computed the differences $\delta Q_\omega^{\rm H,\infty} = Q_\omega^{\rm NR_H} - Q_\omega^{\rm NR_H^\infty}$, $\delta Q_\omega^{\rm HM} = Q_\omega^{\rm NR_H} - Q_\omega^{\rm NR_M}$ and $\delta Q_\omega^{\rm H,n=4} = Q_\omega^{\rm NR_H} - Q_\omega^{\rm NR_{H,\,n=4}}$ and summed them in quadrature, so to estimate the error-bar $\sigma_{Q_\omega^{\rm NR}} = \pm 1/2\sqrt{(\delta Q_\omega^{\rm HM})^2 + (\delta Q_\omega^{\rm H\infty})^2 + \left(\delta Q_\omega^{\rm H,n=4}\right)^2}$ that we represented in Fig. 6. This conservative error estimate is of order unity, as it varies between $(-3,+2)$ at $\omega = 0.0415$, and between $(-1,+1)$ at $\omega = 0.0603$.

Together with the numerical curve we also exhibit in the picture other five analytical EOB curves: the point-mass EOB (dash-dotted, black online), the LO tidal EOB (thick-dashed, blue online), the analytical, 2PN tidal EOB with $\alpha_2^{(2)} = 85/14$ (thick-solid, red online) and the effective 2PN tidal EOB with the *effective* values $\bar\alpha_2 = 40$ and $\bar\alpha_2 = 100$ used in Ref. [19] (lowermost dotted lines, black and magenta online, from top to bottom). The figure highlights clearly the dependence of NR on tidal interaction. One concludes that: (i) the NR curve is always very close to the 2PN tidal EOB one; (ii) it is very well distinguishable from the point-mass prediction; (iii) the error-bar on the NR curve is too large to appreciate the differences between the LO and 2PN tidal EOB models; (iv) the effective 2PN tidal EOB model used in Ref. [19] with $\bar\alpha_2 = 100$ significantly overestimates the magnitude of tidal interactions in the NR data; (v) the effective 2PN tidal EOB model with $\bar\alpha_2 = 40$ gives a good average of the numerical points.

The most important information suggested by Fig. 6 is that the EOB tidal model constructed using *only* analytically computed tidal information is by itself consistent with the NR simulation, *without* the need of tuning any additional tidal EOB flexibility parameter yielding an effective amplification of the tidal interaction as the stars get closer and closer. We can not exclude that such an amplification exists [8], but one will need much higher accuracy in the late inspiral phase to identify actual physical effects. In this respect, although the value $\bar\alpha_2 = 40$ fits well the NR data, it does not indicate definitely an amplification of tidal effects, as truncation errors are still dominant in this frequency range and the value of $\bar\alpha_2$ is very sensitive to small changes on Q_ω that are barely visible on the plot. For instance, note how the EOB Q_ω is easily matching the upper bound of the error-bar by taking $\bar\alpha_2 = 20$. We expect that the use of higher-resolutions and/or more accurate numerical treatments of the hydrodynamics will further move up the NR Q_ω curve, so to favour smaller values of $\bar\alpha_2$ than larger ones.

The (visually) small differences between the Q_ω's in Fig. 6 actually correspond to relevant dephasings, of order 1 *rad* or more. This information, relative to the frequency interval $[\omega_1,\omega_2]M = [0.041, 0.062]$, is quantified in Table II. The 2PN (NNLO) tidal EOB model accumulates a dephasing of 1.06 *rad*, the LO EOB model 1.49 *rad*, while the point-mass EOB 3.92 *rad*. The uncertainties on these numbers are of the order $\sigma_{\Delta\phi} = 0.61$ *rad*, and obtained by integrating the shaded region in Fig. 6.

Due to the fitting procedure involved in the computation of the Q_ω curves [19], it is important to verify the phasing with another diagnostic. Hence, we present also an analysis based on waveform alignment as customary in the literature. The time evolution of the phase difference $\Delta\phi_{22}(t) = \phi^{\rm X}(t) - \phi^{\rm NR}(t)$ (where the label X can be either EOB or T4) is shown in Fig. 7. It is computed from the time-and-phase alignement waveforms, as in Fig. 5. The shaded region represents the uncertainty on the NR phase. The qualitative information given by this plot confirms the analysis of the phasing given by the Q_ω: tidal effects are clearly visible before contact and the current analytical knowledge is sufficient to match the NR phasing up to contact (dashed vertical line in the figure). It is not possible, however, to distinguish in the NR data the effect of higher-order tidal effects from LO ones. Interestingly, on this plot the T4 tidal LO model performs marginally worse than the corresponding EOB model, ~ -0.3 *rad* at contact and notably out of the estimated NR uncertainty. Note that the phase difference varies in

[8] Especially on the basis of the analytical considerations of Ref. [13] suggesting that $\alpha_2^{(2)}$ might be replaced by an effective distance dependent coefficient $\alpha_2^{\rm eff}(u) \equiv \alpha_2^{(2)}/(1 - r_{\rm LR}u)$, $r_{\rm LR}$ denoting the EOB effective light-ring location. Note however that the corrisponding Q_ω curve would be indistingushable from the nonresummed one on the plot.

the range ± 0.2 *rad* from the beginning of the simulation (after the initial burst) up to contact. This value is consistent with lower value $\Delta\phi - \sigma_{\Delta\phi} \sim 0.5$ obtained from Table II. For completeness, in Fig. 7 we also added the two phase differences with the effective 2PN tidal EOB model, with $\bar{\alpha}_2 = 20$ and $\bar{\alpha}_2 = 40$. The are both well within the error bar, although, consistently with the Q_ω analysis, the value $\bar{\alpha}_2 = 20$ actually yields a smaller dephasing at contact. In conclusion, putting together the information of Figs. 6-7, state-of-the art numerical simulations allow us to conclude that, if any actual amplification of tidal effects exists, it yields, conservatively, $\bar{\alpha} < 40$ (as a conservative estimate), or, more likely, $\bar{\alpha}_2 < 20$.

We conclude this Section with a few comments about the accuracy of the higher-order multipoles, that are actually included in the computation of $E^{\rm NR}(j)$. Figure 8 compares the modulus of the most relevant subdominant numerical multipoles $\ell = 3$, $m = 2$ and $\ell = m = 4$ with the corresponding EOB waveforms. To our knowledge, this comparison has never been shown before. The visual agreement is rather good, with both analytical multipoles averaging the corresponding numerical ones practically up to contact, as it was the case for the $\ell = m = 2$ case. From the picture one also sees the large initial burst of junk radiation that must be included in the accurate computation of the $E^{\rm NR}(j)$ relation.

V. CONCLUSIONS

In this paper we have presented a comparison between dynamics and waveform from BNS coalescence computed from long-term ($\sim$ ten orbits) NR simulations and the tidal EOB model including all the known tidal PN corrections [13].

New numerical simulations have been presented which improve quantitatively previous results [18]. A set of simulations which employ the same initial data, grid setup, and resolutions of [18], but adopt an higher-order reconstruction method in the HRSC scheme and time integrator, has shown that tidal effects can be overestimated by numerical inaccuracies. While the data show convergent behavior before the contact, around this point and later the uncertainties related to numerical viscosity do not seem completely under control, and actually become dominant over truncation errors.

In order to compare NR data with the analytical EOB model, we estimated the GW frequency of the contact as, $M\omega_{22}^{c} \sim 0.078$.

The dynamics of the system has been investigated by means of the $E(j)$ relation between the reduced binding energy E and the reduced angular momentum j, computed here for the first time for BNS simulations and presented in Fig. 4. The tidal EOB model is consistent with the NR data up to contact ($j = 3.63$) and even later, up to $j \sim 3.5$.

The effects of tidal interactions are clearly visible in the NR/EOB waveforms. The comparison of amplitude and frequency (Fig. 5) indicates that tidal effect become significant in the very late part of the inspiral, just before contact. Given the uncertainties on the NR data, it is not possible to meaningfully disentangle 1PN (NLO) and 2PN (NNLO) tidal corrections from the LO ones. The T4 tidal model with LO tidal corrections is slightly worse (-0.3 rad) than the EOB model when getting close to contact. The phasing was studied by means of both a gauge-invariant, frequency-based analysis employing the Q_ω diagnostic [19] and a standard time and phase-shift alignment procedure. The results of the former method are collected in Fig. 6 and Table II, the ones of the latter in Fig. 7. The Q_ω diagnostic is more affected by the noise of the data which results in somehow larger uncertainties; the time and phase alignment suffers of ambiguities in the choice of the interval and potentially underestimates actual differences accumulated up to the alignment interval. In summary, while they give slightly different numbers, the picture emerging from the two phasing analyses is consistent: tidal effects are clearly visible during the late inspiral up to contact and the current analytical knowledge is sufficient to match the NR phasing. It is not possible, however, to distinguish in the NR data the effect of higher-order tidal effects from LO ones. We observe that after contact and up to merger (i.e., for about one further orbit), the 2PN EOB model performs better than any other analytical tidal model; note however that the extension of any analytical model beyond contact has only an effective meaning.

In conclusion, we have shown that the current analytic knowledge incorporated into the EOB model is sufficient to reproduce within the uncertainties the numerical data up to contact. No calibration of any tidal effective-one-body free parameter is required, beside those already fitted to binary black holes data. While the 2PN (NNLO) model minimizes the differences with the NR data, it is not possible to significantly distinguish it from the 1PN (LO) model. Obviously, we cannot exclude the presence of a further amplification of tidal interaction as the star gets close (as suggested by Ref. [13]), but the present NR data indicate that this effect, if present, is *smaller* than what believed in the past [19] (i.e. $\bar{\alpha_2} = 100$) and it is not possible to estimate it precisely. A conservative analysis points points to $\bar{\alpha}_2 < 40$, though we think that a more likely estimate (at one-sigma level) is $\bar{\alpha}_2 < 20$. Note in addition that for higher, more realistic compactnesses (say $\mathcal{C} = 0.16 - 0.18$) tidal effects are even smaller, thus potentially more difficult to extract from the numerical data. Similar considerations also hold for the use of realistic EOS, which present their own numerical challanges to be used in NR simulations.

As a consequence, the 2PN-accurate tidal EOB model [13] used in this work [9] should be considered in the future as the most reliable choice to produce exact/target

[9] Here we focused on the equal-mass case only, but we expect this EOB model to be accurate in the range of plausible mass

data for the development of templates for data-analysis purposes [6].

This work also pointed out the importance of extensive numerical tests to assess the uncertainties of the numerical data, and the potential need of new numerical strategies to perform accurate simulations. Considering that the simulations presented here are the longest and employ the among the highest resolutions to date, error assessment and convergence tests appear absolutely necessary in future studies of this kind. Because the use of significantly higher resolutions (e.g. $\sim 400^3$ points covering each star) and extensive tests seem to be computationally unfeasible, the development of alternative and more accurate numerical methods seems unvoidable to further improve and confirm our results.

ACKNOWLEDGMENTS

We warmly thank T. Damour for prompting this research and for a careful reading of the manuscript. This work was supported in part by DFG grant SFB/Transregio 7 "Gravitational Wave Astronomy". SB thanks IHES for hospitality during the development of part of this work. Computations were performed on JuRoPA (JSC), SuperMUC (LRZ), and Louhi (CSC) clusters. Computer time in Louhi was granted by PRACE Tier-1.

[1] T. Damour, Phys.Rev.Lett. **51**, 1019 (1983)
[2] T. Hinderer, Astrophys.J. **677**, 1216 (2008), arXiv:0711.2420 [astro-ph]
[3] T. Damour and A. Nagar, Phys. Rev. **D79**, 081503 (2009)
[4] T. Binnington and E. Poisson, Phys.Rev. **D80**, 084018 (2009), arXiv:0906.1366 [gr-qc]
[5] T. Hinderer, B. D. Lackey, R. N. Lang, and J. S. Read, Phys.Rev. **D81**, 123016 (2010), arXiv:0911.3535 [astro-ph.HE]
[6] T. Damour, A. Nagar, and L. Villain(2012), 28 pages, 6 figures. Submitted to Phys. Rev. D, arXiv:1203.4352 [gr-qc]
[7] T. Damour and A. Nagar, Phys.Rev. **D81**, 084016 (2010), arXiv:0911.5041 [gr-qc]
[8] A. Buonanno and T. Damour, Phys. Rev. **D59**, 084006 (1999)
[9] A. Buonanno and T. Damour, Phys. Rev. **D62**, 064015 (2000)
[10] T. Damour, P. Jaranowski, and G. Schaefer, Phys. Rev. **D62**, 084011 (2000)
[11] T. Damour, B. R. Iyer, and A. Nagar, Phys. Rev. **D79**, 064004 (2009)
[12] J. E. Vines and E. E. Flanagan(2010), arXiv:1009.4919 [gr-qc]
[13] D. Bini, T. Damour, and G. Faye(2012), arXiv:1202.3565 [gr-qc]
[14] J. Vines, E. E. Flanagan, and T. Hinderer, Phys.Rev. **D83**, 084051 (2011), arXiv:1101.1673 [gr-qc]
[15] T. Damour and A. Nagar, Phys.Rev. **D80**, 084035 (2009), arXiv:0906.0096 [gr-qc]
[16] J. S. Read, C. Markakis, M. Shibata, K. Uryu, J. D. Creighton, *et al.*, Phys.Rev. **D79**, 124033 (2009), arXiv:0901.3258 [gr-qc]
[17] L. Baiotti, T. Damour, B. Giacomazzo, A. Nagar, and L. Rezzolla, Phys.Rev.Lett. **105**, 261101 (2010), arXiv:1009.0521 [gr-qc]
[18] S. Bernuzzi, M. Thierfelder, and B. Brügmann(2011), arXiv:1109.3611 [gr-qc]
[19] L. Baiotti, T. Damour, B. Giacomazzo, A. Nagar, and L. Rezzolla, Phys.Rev. **D84**, 024017 (2011), arXiv:1103.3874 [gr-qc]
[20] T. Damour, A. Nagar, D. Pollney, and C. Reisswig, Phys.Rev.Lett. **108**, 131101 (2012), 4 pages, 2 figures, arXiv:1110.2938 [gr-qc]
[21] Y. Pan, A. Buonanno, M. Boyle, L. T. Buchman, L. E. Kidder, *et al.*, Phys.Rev. **D84**, 124052 (2011), 26 pages, 25 figures, published Phys. Rev. D version, arXiv:1106.1021 [gr-qc]
[22] T. Damour and O. M. Lecian, Phys. Rev. D **80**, 044017 (2009)
[23] J. A. Faber and F. A. Rasio(2012), arXiv:1204.3858 [gr-qc]
[24] B. Giacomazzo, L. Rezzolla, and L. Baiotti, Phys.Rev. **D83**, 044014 (2011), arXiv:1009.2468 [gr-qc]
[25] M. Thierfelder, S. Bernuzzi, and B. Brügmann, Phys.Rev. **D84**, 044012 (2011), arXiv:1104.4751 [gr-qc]
[26] K. Taniguchi and E. Gourgoulhon, Phys.Rev. **D66**, 104019 (2002), arXiv:gr-qc/0207098 [gr-qc]
[27] B. Brügmann, W. Tichy, and N. Jansen, Phys.Rev.Lett. **92**, 211101 (2004), arXiv:gr-qc/0312112 [gr-qc]
[28] B. Brügmann, J. A. Gonzalez, M. Hannam, S. Husa, U. Sperhake, *et al.*, Phys.Rev. **D77**, 024027 (2008), arXiv:gr-qc/0610128 [gr-qc]
[29] L. Del Zanna and N. Bucciantini, Astron. Astrophys. **390**, 1177 (2002), arXiv:astro-ph/0205290
[30] R. Borges, M. Carmona, B. Costa, and W. S. Don, Journal of Computational Physics **227**, 3191 (2008), ISSN 0021-9991, http://www.sciencedirect.com/science/article/pii/S002199
[31] C. Reisswig and D. Pollney, Class.Quant.Grav. **28**, 195015 (2011)
[32] T. Damour, A. Nagar, D. Pollney, and C. Reisswig, in preparation(2012)

ratios for a BNS system, from $M_A/M_B = 1$ to $M_A/M_B = 0.7$, corresponding to $\nu \in [0.2422, 0.25]$. The reason for this being the fact that the EOB model used here was found consistent with (now relatively old) BBH data up to 2:1 mass ratio ($\nu = 2/9 = 0.2222$). Further improvements of the current EOB point-mass model are currently in progress [32], consistently with the finding of Ref. [21].

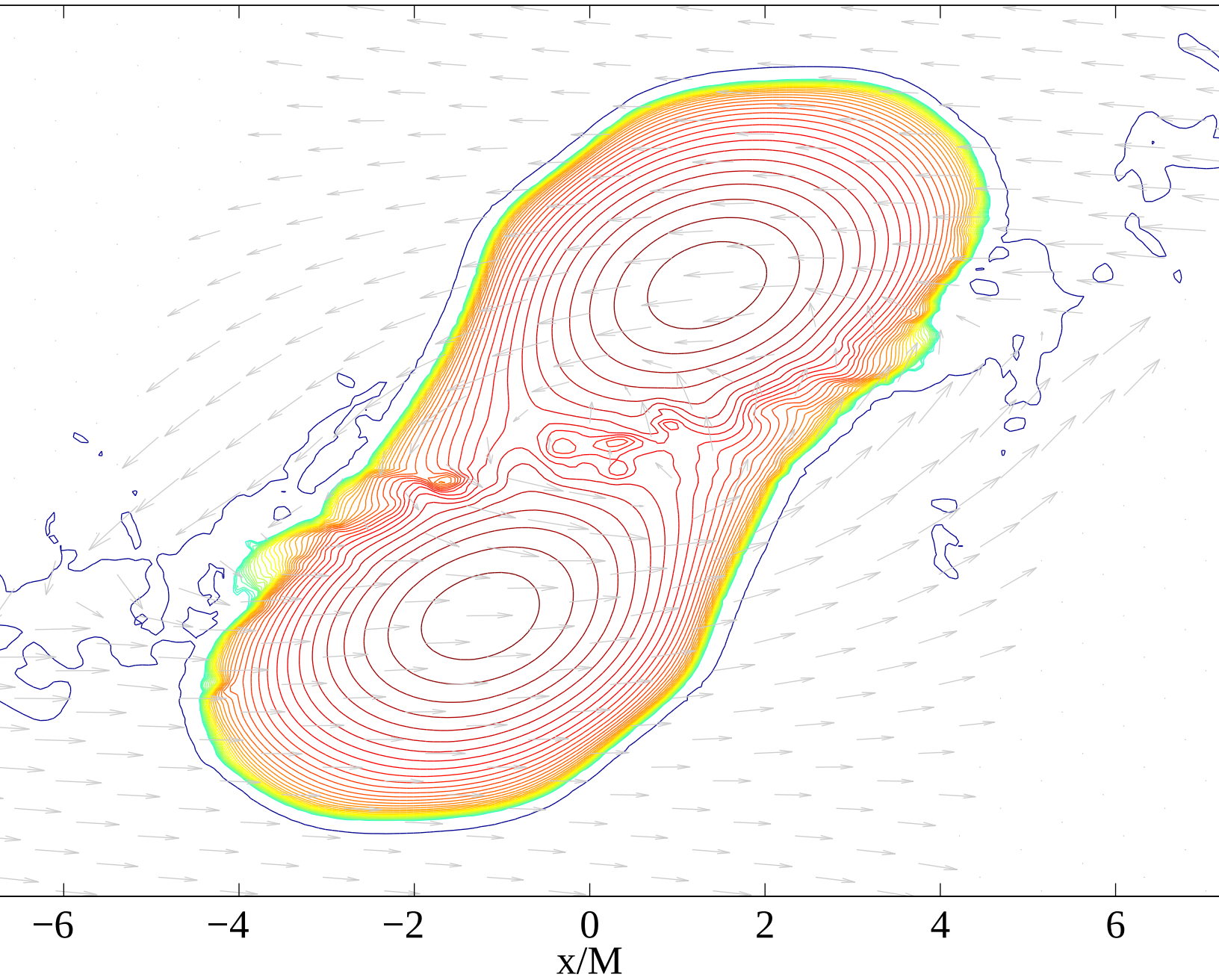
−6
−4
−2
0
2
4
6
x/M

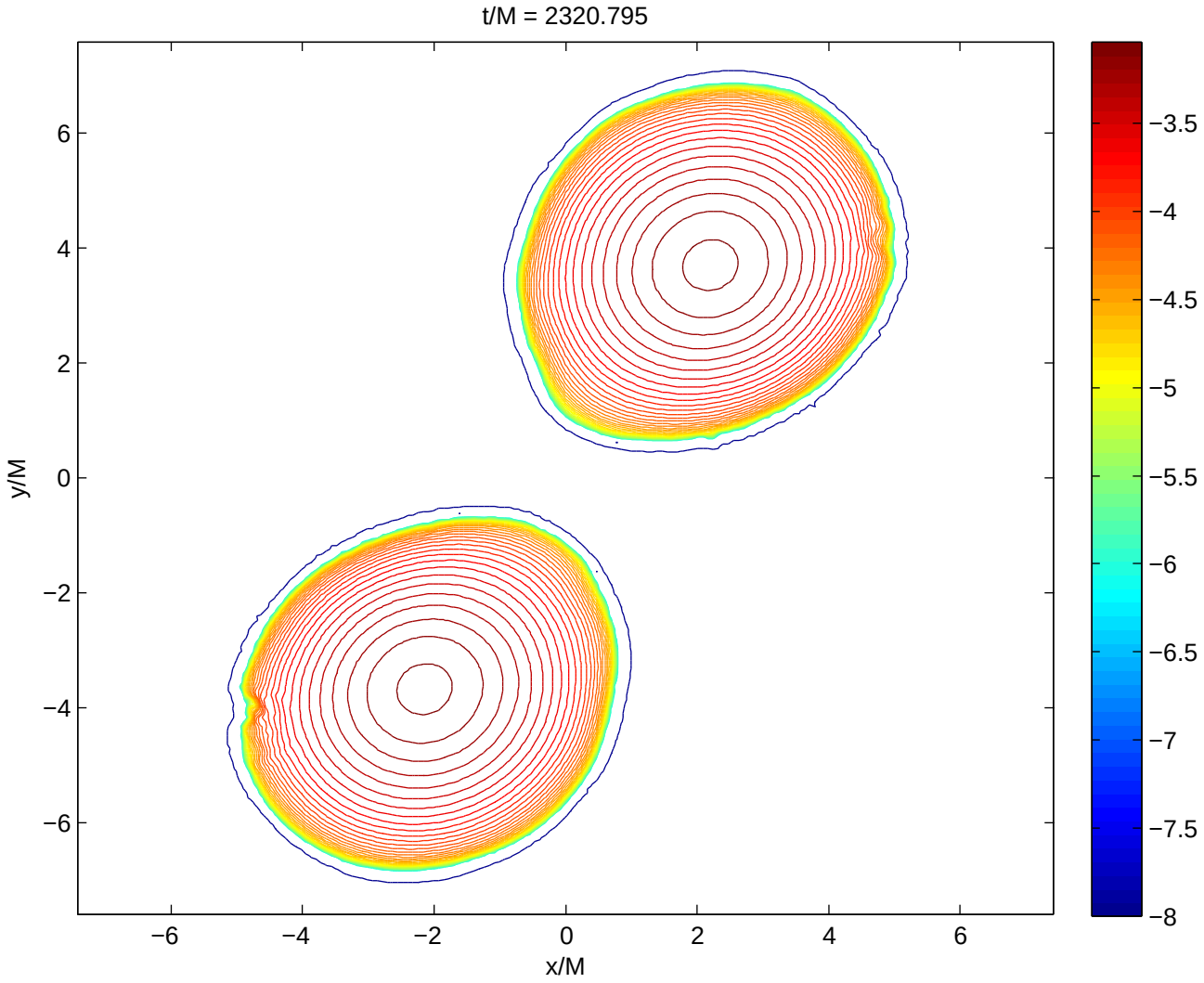
t/M = 2320.795
y/M
x/M
6
4
2
0
−2
−4
−6
−6
−4
−2
0
2
4
6
−3.5
−4
−4.5
−5
−5.5
−6
−6.5
−7
−7.5
−8

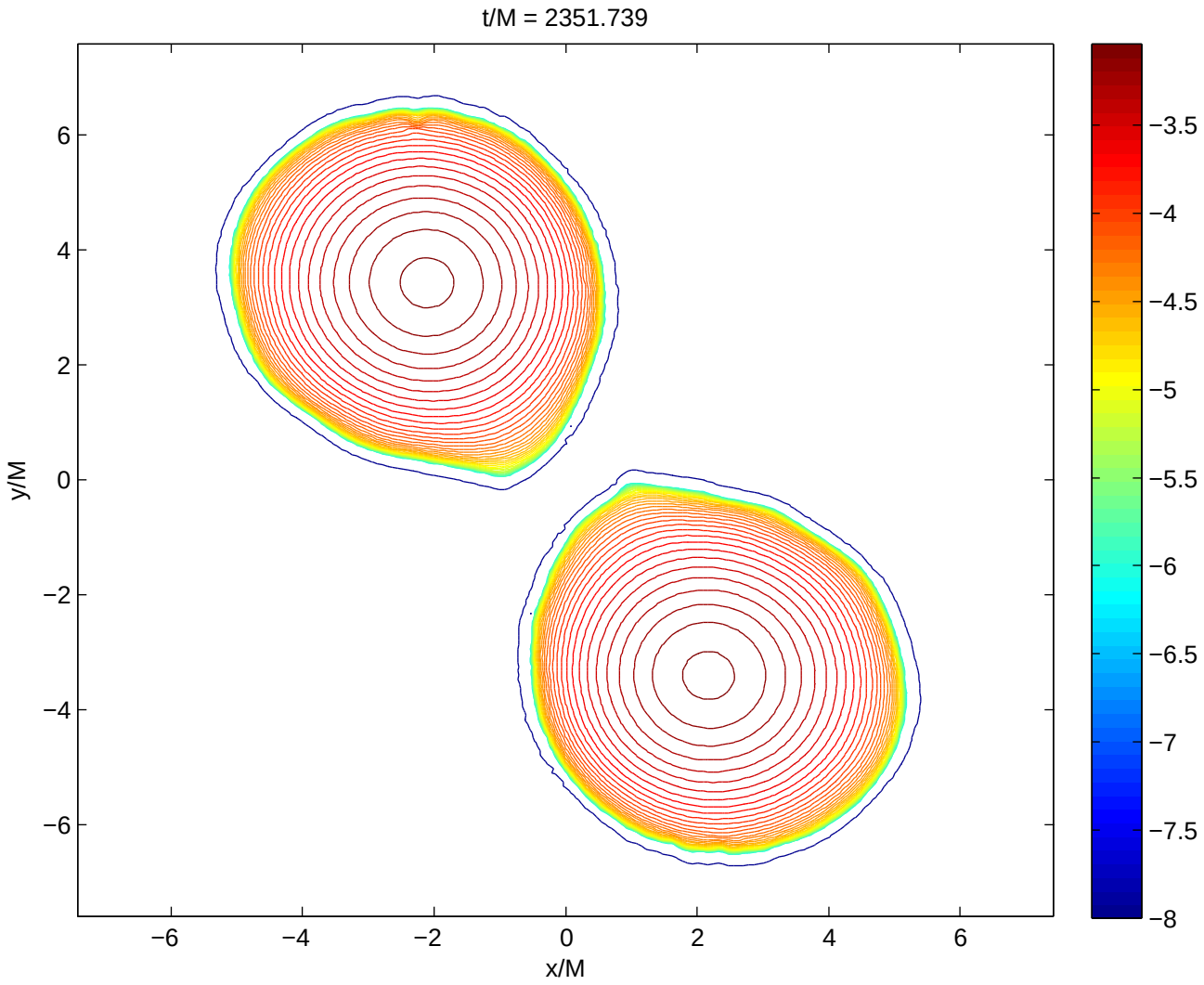
t/M = 2351.739
y/M
x/M
6
4
2
0
−2
−4
−6
−6
−4
−2
0
2
4
6
−3.5
−4
−4.5
−5
−5.5
−6
−6.5
−7
−7.5
−8

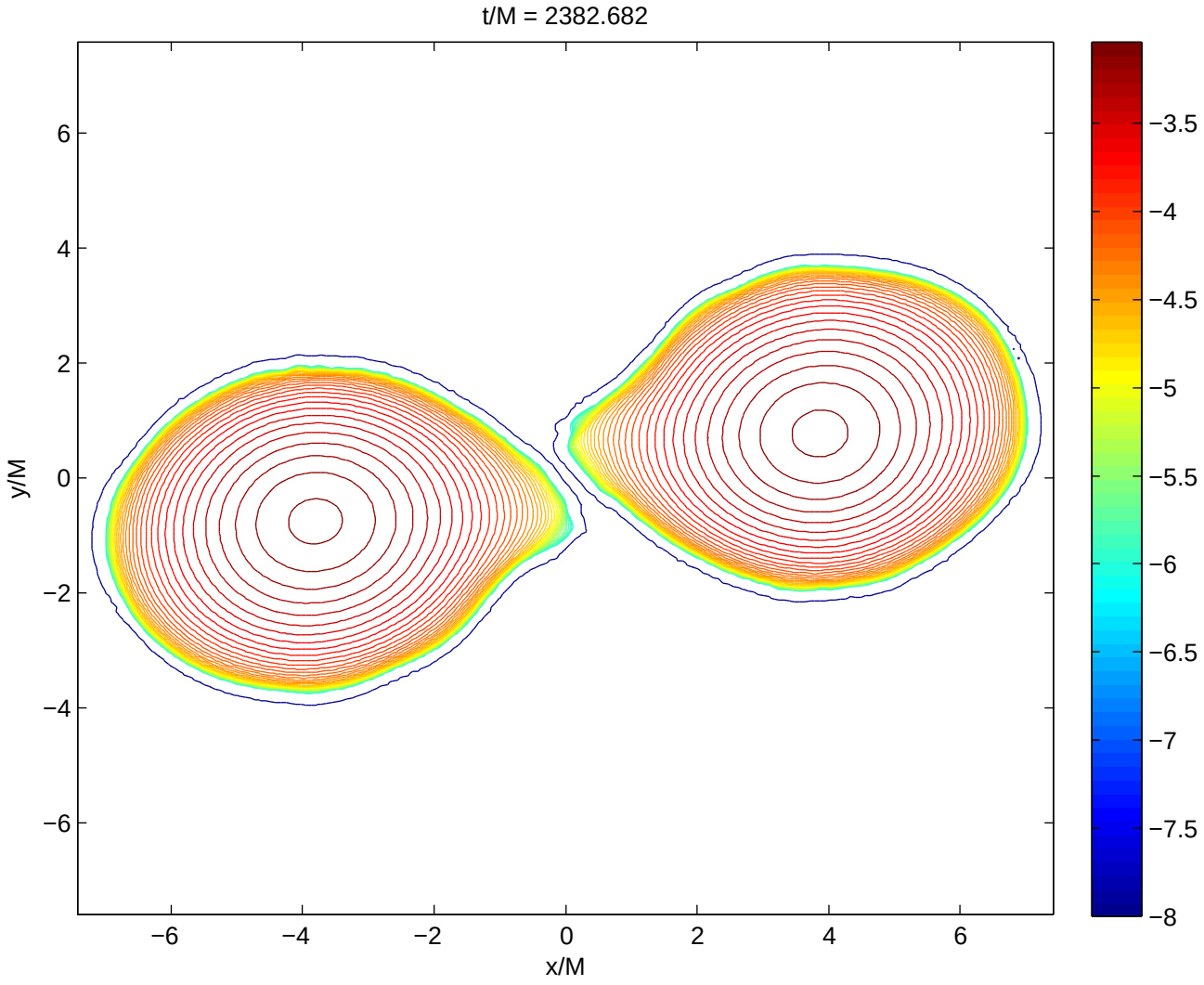
t/M = 2382.682
y/M
x/M
6
4
2
0
−2
−4
−6
−6
−4
−2
0
2
4
6
−3.5
−4
−4.5
−5
−5.5
−6
−6.5
−7
−7.5
−8

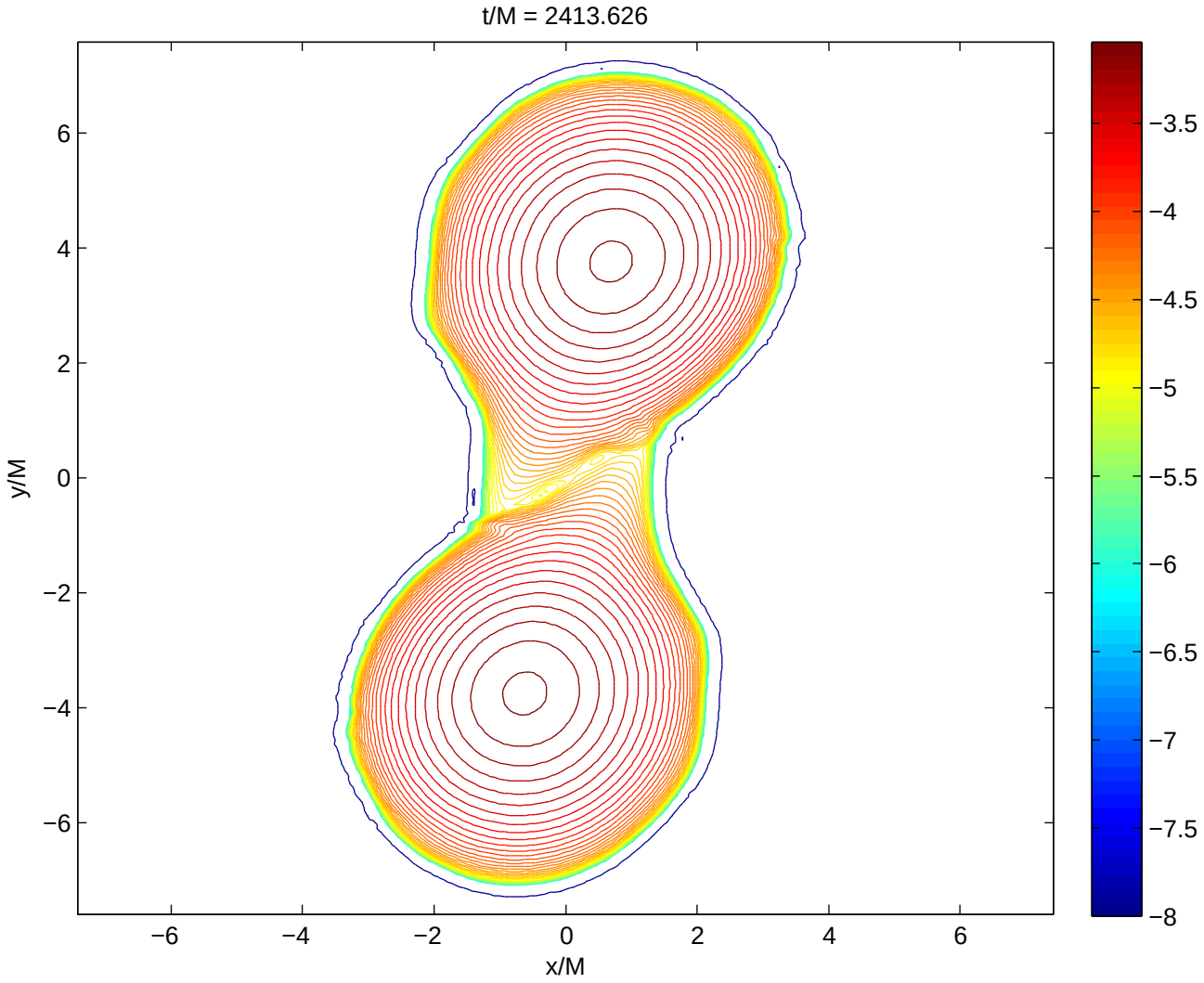
t/M = 2413.626
y/M
x/M
6
4
2
0
−2
−4
−6
−6
−4
−2
0
2
4
6
−3.5
−4
−4.5
−5
−5.5
−6
−6.5
−7
−7.5
−8